International Journal of Solids and Structures 102–103 (2016) 176–185

Contents lists available at ScienceDirect

International Journal of Solids and Structures

journal homepage: www.elsevier.com/locate/ijsolstr

Global and local interactive buckling behavior of a stiff film/compliant substrate system

C.G. Wang[a,b,*], Y.P. Liu[a,*], H.F. Tan[a,b]

[a] Center for Composite Materials, Harbin Institute of Technology, Harbin 150001, China
[b] National Key Laboratory of Science and Technology on Advanced Composites in Special Environments, Harbin Institute of Technology, Harbin 150080, China

ARTICLE INFO

Article history:
Received 14 May 2016
Revised 12 September 2016
Available online 15 October 2016

Keywords:
Global and local buckling
Thin film
Second bifurcation
Snap-back
Path-following technique

ABSTRACT

This paper elucidates the global and local interactive buckling behavior of a stiff film resting on a compliant substrate under uniaxial compression. The resulting governing non-linear equations (non-autonomous fourth-order ordinary differential nonlinear equations with integral conditions) are then solved by introducing a continuation algorithm, which offers considerable advantages to detect multiple bifurcations and trace a complex post-buckling path. The critical conditions for local and global buckling and respective post-buckling equilibrium paths are carefully studied. Two different evolution mechanisms of buckling modes and processes from destabilization to restabilization (snap-back) are observed beyond the onset of the primary sinusoidal wrinkling mode in the post-buckling range. In addition, the shear modulus of an orthotropic substrate acts as a dominant role in the bifurcation portrait. Our results offer better understanding of the global and local buckling behaviors of such a bilayer system, and can open up new opportunities for the design and applications of novel nanoelectronics.

1. Introduction

Bilayer systems consisting of a stiff thin film on a compliant substrate have provoked a surge of research interest in academic domains over the last decade (Bowden et al., 1998; Huang and Suo, 2002; Schweikart and Fery, 2009). When such a system is subjected to a large compression, it may lose its original flat surface and leads to buckling, which may dramatically alter their inherent structural equilibrium and thus results in a series of changes in properties (Efimenko et al., 2005; Koch et al., 2009; Wang et al., 2013a). As such, the film/substrate system in the post-buckling state has potential uses as stretchable electronic devices, tunable diffraction and phase gratings or patterned platforms for cell adhesion (Harrison et al., 2004; Stafford et al., 2004; Rogers et al., 2010).. Many previous studies have shown that a number of possible post-buckling morphologies may occur in the surface, including global buckling, sinusoidal, checkerboard, herringbone, etc (Chen and Hutchinson, 2004; Cai et al., 2011; Wang et al., 2013b; Xu et al., 2015). How to comprehensively evaluate these possible morphologies, as well as their relationship and formation mechanism, remains a challenge (Li et al., 2012).

Thus far, several theoretical approaches, such as linear perturbation analysis and non-linear buckling analysis, have been proposed and become effective means for exploring the instability behavior of the systems (Wang et al., 2008; Im and Huang, 2008; Zhuo and Zhang, 2015). However, most of these studies have focused on the critical load and morphologies at the initial stage of instability threshold. There is a lack of investigation on the morphological evolution and mode transition in the post-buckling stage due to incredibly complication, such as geometrical and material nonlinearities, loading path dependence, etc. Therefore, reliable numerical solution techniques for tracing and branch switching post-buckling response of film/substrate system are in demand.

Recent efforts have been devoted to such post-buckling analysis by using finite element methods (Sun et al., 2012; Cao et al., 2012), which is more flexible to describe complicated geometries and boundary conditions. However, the simulation may not capable to trace a more complex case, especially whose post-buckling path is accompanied with snap-back or snap-through phenomenon due to the presence of secondary instabilities such as local buckling. Information about bifurcations is not immediately available to the user and stopping and restarting the simulation at a fixed point is not straightforward (Pirrera et al., 2010; Ke et al., 2016).

For all of the aforementioned reasons, we adopted a continuation algorithm to solve the resulting non-linear equations, in consideration of possible bifurcations along the equilibrium path

* Corresponding authors.
E-mail addresses: wangcg@hit.edu.cn (C.G. Wang), liuyp@hit.edu.cn (Y.P. Liu).

http://dx.doi.org/10.1016/j.ijsolstr.2016.10.006
0020-7683/

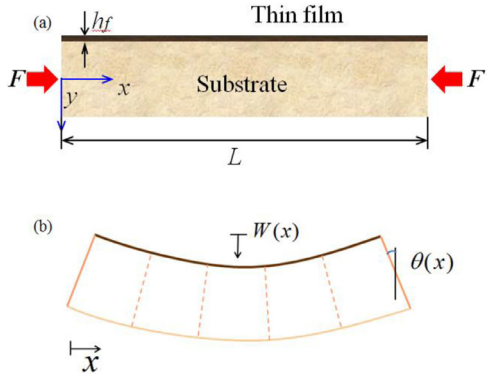

Fig. 1. (a) Illustration of a film/substrate system under compression; (b) Sway and tilt components.

tracing of the non-linear response of a system. It appears as a significantly efficient path-following technique with two key features, the detection of bifurcation points and the branch-switching from one equilibrium path to another bifurcation path, and has been demonstrated to be an efficient technique to deal with various non-linear problems in solid mechanics (Damil and Potier-Ferry, 1990; Wadee and Hunt, 1998; Abichou et al., 2002; Wadee et al., 2015). The following problem thereby can be computed by coupling analytical models with the continuation algorithm.

In this paper, a comprehensive study of the global and local instability behaviors in film/substrate systems is provided from a continuum mechanics perspective. The study is structured as follows. In Section 2, the buckling governing equations, taking account of the global and local deformations are established. The aim here is to describe different morphologies of the film/substrate under compression. In Section 3, the resulting governing equations are solved by introducing a continuation algorithm to trace the whole equilibrium paths and obtain post-buckling characteristics of the systems. Section 4 presents the results, including the critical condition for local and global buckling, the respective post-buckling equilibrium paths and mode evolutions. Finally, the effects on bifurcation portrait of orthotropic substrate are discussed.

2. Model formulation

In this work we investigate the instability behavior of an isotropic stiff film with a thickness of h_f on a soft orthotropic substrate. The compliant substrate has different Young's moduli in the axial direction *Ex* and the transverse direction *Ey* and an associated shear modulus *G* with a finite thickness of h_s and a length of L_x. Poisson's ratios in the x- and y-directions are *vx* and *vy*, respectively. The structural parameters are described by a Cartesian coordinate system, where the longitudinal direction and the transverse horizontal direction are determined as the x-axis and the y-axis, respectively (Fig. 1(a)). The bilayer system deforms in the x-y plane and distributes uniformly along z-axis (perpendicular to the x-y plane). A steady axial compressive force *F* is applied at each side of the substrate.

Different instability phenomena may occur in this bilayer system, including global buckling, local wrinkling and their interactive buckling. In order to describe these complicated instability phenomena, the formulation of the model is described through both the global and the local modal displacements. Firstly, two dimensionless factors are introduced to present the global sway and tilt, i.e., q_s and q_t, directly to describe the shear effect (Fig. 1(b)), which has a great effect on the formation of local buckling.

Here q_s not necessarily equals q_t, which is different from the Euler model where the two are assumed to be identical. Then, the global sway $W(z)$ and tilt $\theta(z)$ can be approximated as the following expressions (Bai and Wadee, 2015; Wang et al., 2016):

$$W(x) = q_s L \sin\frac{\pi x}{L}$$
$$\theta(x) = q_t \pi \cos\frac{\pi x}{L}. \tag{1}$$

Thus the corresponding shear strain is given by:

$$\gamma_{xy}(x) = (q_s - q_t)\pi \cos\frac{\pi x}{L}. \tag{2}$$

Secondly, local wrinkling deformation is described by two functions $u_f(x)$ and $w_f(x)$, for the local in-plane and transverse displacements, respectively. It is noted that these functions have no phenomenological assumptions and are sought as solutions from minimization of total potential energy. Therefore, they can well describe the buckling evolution without wrinkling pattern or number restriction.

The total potential energy of the system, Π, is mainly composed of bending energy, U_B, membrane energy, U_M, elastic strain energy of the substrate, U_S, and work done by load, U_L, and is expressed as follows:

$$\Pi = U_B + U_M + U_S - U_L. \tag{3}$$

The bending energy of the thin film is due to the collective effect of global and local deformations, and can be expressed as:

$$U_B = \frac{1}{2}EI\int_0^{L_x}(\ddot{W}^2 + \ddot{w}_f^2)\mathrm{d}x$$
$$= \frac{1}{2}EI\int_0^{L_x}\left(2q_s^2\frac{\pi^4}{L^2}\sin^2\frac{\pi x}{L} + \ddot{w}_f^2\right)\mathrm{d}x. \tag{4}$$

where $EI = \frac{E_f L_z h_f^3}{12(1-v_f^2)}$ is the flexural rigidity of the film; L_z denotes the breadth of the film; E_f and v_f are Young's modulus and Poisson's ratio, respectively. In addition, the notation "dot" above the variables denotes a spatial derivatived/dx.

Along with bending energy, the film is also subjected to membrane action. When nonlinear large deformation is taken into account, the total membrane energy can be expressed as follows according to the von Kármán hypothesis:

$$U_M = \frac{1}{2}E_f h_f L_z\int_0^{L_x}(\varepsilon_x)^2\mathrm{d}x$$
$$= \frac{1}{2}E_f h_f L_z\int_0^{L_x}(\frac{1}{2}h_s\dot{\theta} - \Delta + \dot{u} + \frac{1}{2}\dot{w}^2)^2\mathrm{d}x. \tag{5}$$

where $\frac{1}{2}h_s\dot{\theta}$ is the axial strain term corresponding to the global buckling, $\dot{u} + \frac{1}{2}\dot{w}^2$ is the axial strain term corresponding to the local wrinkling deformation, Δ is the axial strain term corresponding to purely uniform compressive strain, which contributes to the pre-buckling equilibrium path.

As the system generally has an extremely large ratio of Young's modulus ($E_f/E_s \approx 10^5$), the terms for the axial strain energy in the substrate are assumed to be small compared to the membrane energy in the film. Therefore, the substrate provides only a small proportion of the axial resistance, but the main resistance to local transverse displacement and shear deformation (Wadee and Hunt, 1998; Audoly and Boudaoud, 2008). Further justification will

be discussed in detail in Section 4.3. The strain vector $\{\boldsymbol{\gamma}\}$ of the substrate can be obtained by taking the global and local collective effects into account, and is expressed as:

$$\{\boldsymbol{\gamma}\}=\begin{Bmatrix} \dfrac{\partial u_s}{\partial x}+\dfrac{1}{2}\left(\dfrac{\partial w_s}{\partial x}\right)^2-y\dfrac{d\theta}{dx}-\Delta \\ v_x\Delta+\dfrac{\partial w_s}{\partial y} \\ (q_s-q_t)\pi\cos\dfrac{\pi x}{L}+\dfrac{\partial w_s}{\partial x}+\dfrac{\partial u_s}{\partial y} \end{Bmatrix}. \tag{6}$$

A plane-stress assumption is used to model the strain energy of the substrate ($\sigma_z=\tau_{xz}=\tau_{yz}=0$). Therefore, the elastic strain energy of the substrate U_S is obtained as:

$$U_s=\int_0^{L_x}\int_0^{h_s}\{\boldsymbol{\gamma}\}^*[\mathbf{Q}^s]\{\boldsymbol{\gamma}\}dxdy, \tag{7}$$

where

$$[\mathbf{Q}^s]=\begin{bmatrix} \dfrac{E_xL_z}{2(1-\nu_x\nu_y)} & \dfrac{E_y\nu_xL_z}{2(1-\nu_x\nu_y)} & 0 \\ \dfrac{E_x\nu_yL_z}{2(1-\nu_x\nu_y)} & \dfrac{E_yL_z}{2(1-\nu_x\nu_y)} & 0 \\ 0 & 0 & \dfrac{GL_z}{2} \end{bmatrix}. \tag{8}$$

To ensure continuity of the displacements between the film and substrate, and simplify the following buckling governing equations (partial differential equations) to ordinary differential equations, the local wrinkling mode is assumed to vary linearly with y, such that the bottom of substrate has no local displacement.

$$\begin{aligned} w_s(x,y)&=\left(\frac{h_s-2y}{2h_s}\right)w_f(x) \\ u_s(x,y)&=\left(\frac{h_s-2y}{2h_s}\right)u_f(x). \end{aligned} \tag{9}$$

The final component of total potential energy is the work done by the external load, F, which is the sum of the energy contributions from the local wrinkling, pure compression and sway from global buckling. Then the work done by load can be expressed as:

$$U_L=\int_0^{L_x}F\left(\frac{1}{2}\dot{W}^2-\frac{1}{2}\dot{u}_f+\Delta\right)\mathrm{d}x. \tag{10}$$

Therefore, the total potential, Π, can be expressed as:

$$\Pi=\int_0^L\left\{\begin{aligned} &\frac{1}{2}EI(\ddot{w}_f^2+q_s^2\frac{\pi^4}{L_x^2}\sin^2\frac{\pi x}{L_x})+D[\Delta^2+q_t^2\frac{h_s^2\pi^4}{4L_x^2}\sin^2\frac{\pi x}{L_x}-(\dot{u}_f+\frac{1}{2}\dot{w}_f^2)(2\Delta \\ &+q_t\frac{h_s\pi^2}{L_x}\sin\frac{\pi x}{L_x})+\dot{u}_f^2+\frac{1}{4}\dot{w}_f^4+q_t\Delta\frac{h_s\pi^2}{L_x}\sin\frac{\pi x}{L_x}+\dot{u}_f\dot{w}_f^2]+Q_{11}^sh_s[\Delta^2-\Delta\dot{u}_f \\ &+q_t^2\frac{h_s^2\pi^2}{12L_x^2}\sin^2\frac{\pi x}{L_x}+\frac{1}{3}\dot{u}_f^2+\frac{1}{20}\dot{w}_f^4-\frac{1}{3}\Delta\dot{w}_f^2+\frac{1}{4}\dot{u}_f\dot{w}_f^2-q_t\frac{h_s^2\pi^2}{6L_x}\sin\frac{\pi x}{L_x}(\dot{u}_f \\ &+\frac{1}{2}\dot{w}_f^2)]+\frac{1}{2}\frac{Q_{22}^s}{h_s}w_f^2+Q_{33}^sh_s[\frac{u_f^2}{h_s^2}+\frac{1}{3}\dot{w}_f^2-\frac{u_f\dot{w}_f}{h_f}+(q_s-q_t)^2\pi^2\cos^2\frac{\pi x}{L_x} \\ &+(q_s-q_t)\pi\cos^2\frac{\pi x}{L_x}(\dot{w}_f-\frac{2}{h_s}u_f)]+Q_{12}^s[\nu_x\Delta h_s(\dot{u}_f-\Delta+\frac{1}{3}\dot{w}_f^2)-(\dot{u}_fw_f \\ &+\frac{1}{3}w_f\dot{w}_f^2)]-F(q_s^2\frac{\pi^2}{2}\cos^2\frac{\pi x}{L_x}-\frac{1}{2}\dot{u}_f+\Delta) \end{aligned}\right\}dx. \tag{11}$$

According to the stability theory, the potential energy, Π, must be stationary at an equilibrium point, that is, $\delta\Pi=0$ for arbitrary $\delta w_f=0$ and $\delta u_f=0$. When integration by parts is performed on Eq. (11) together with variation method, two buckling governing differential equations are obtained. Specifically, $\delta\Pi/\delta w_f=0$ recovers the equilibrium equation in the transverse direction:

$$\begin{aligned} &EI\ddddot{w}_f+D[2\Delta\ddot{w}_f+q_t\frac{h_s\pi^2}{L_x}(\sin\frac{\pi x}{L_x}\ddot{w}_f+\frac{\pi}{L_x}\cos\frac{\pi x}{L_x}\dot{w}_f) \\ &-(2\ddot{u}_f\dot{w}_f+2\dot{u}_f\ddot{w}_f+3\dot{w}_f^2\ddot{w}_f)]+Q_{33}^sh_s[\frac{\dot{u}_f}{h_s}-\frac{2}{3}\ddot{w}_f \\ &+(q_s-q_t)\frac{\pi^2}{L_x}\sin\frac{\pi x}{L_x}]+\frac{Q_{22}^s}{h_s}w_f+Q_{11}^sh_s[\frac{2}{3}\Delta\ddot{w}_f \\ &-(\frac{1}{2}\ddot{u}_f\dot{w}_f+\frac{1}{2}\dot{u}_f\ddot{w}_f+\frac{3}{5}\dot{w}_f^2\ddot{w}_f)+q_t\frac{h_s\pi^2}{6L_x}(\sin\frac{\pi x}{L_x}\ddot{w}_f \\ &+\frac{\pi}{L_x}\cos\frac{\pi x}{L_x}\dot{w}_f)]+Q_{12}^s[\frac{2}{3}(w_f\ddot{w}_f \\ &+\dot{w}_f^2)-\frac{2}{3}\nu_x\Delta h_s\ddot{w}_f-(\dot{u}_f+\frac{1}{3}\dot{w}_f^2)]=0. \end{aligned} \tag{12}$$

Furthermore, $\delta\Pi/\delta u_f=0$ leads to the in-plane equilibrium equation:

$$\begin{aligned} &\left(D+\frac{Q_{11}^sh_s}{3}\right)\ddot{u}_f-\frac{Q_{33}^s}{h_s}u_f+\frac{Q_{33}^s}{2}\dot{w}_f+\left(D+\frac{Q_{11}^sh_s}{4}\right)\dot{w}_f\ddot{w}_f \\ &+\pi\cos\frac{\pi x}{L_x}\left[Q_{33}^s(q_s-q_t)-q_t\frac{h_s\pi^2}{2L_x^2}\left(D+\frac{Q_{11}^sh_s}{6}\right)-\frac{1}{2}Q_{12}^s\dot{w}_f\right]=0. \end{aligned} \tag{13}$$

Compared to the classical equilibrium equations, both global (q_s, q_t and Δ) and local deformations (w_f and u_f) are taken into account in the two equilibrium equations, and the global and local interactions can be considered.

Additionally, we minimize, Π, with respect to the parameters q_s, q_t and Δ, that is, $\frac{\partial\Pi}{\partial q_s}=0$, $\frac{\partial\Pi}{\partial q_t}=0$ and $\frac{\partial\Pi}{\partial\Delta}=0$, give rise to three integral constraints:

$$\begin{aligned} \frac{\partial\Pi}{\partial q_s}&=2Q_{33}^sh_s(q_s-q_t)\pi L_x+q_s\frac{\pi^3EI}{L_x}-Fq_s\pi L_x \\ &+\int_0^{L_x}2Q_{33}^sh_s\cos\frac{\pi x}{L_x}\left(\dot{w}_f-\frac{2}{h_s}u_f\right)dx=0, \end{aligned} \tag{14}$$

$$\frac{\partial \Pi}{\partial q_t} = \left(\frac{D}{2} + \frac{Q_{11}^s h_s}{6}\right) q_t - \frac{2Q_{33}^s L_x^2}{h_s^2 \pi^2}(q_s - q_t) + \int_0^{L_x} \begin{bmatrix} \frac{2Q_{33}^s L_x}{h_s \pi^3} \cos\frac{\pi x}{L_x}\left(\frac{2}{h_s} u_f - \dot{w}_f\right) \\ -\frac{\frac{D}{2} + \frac{Q_{11}^s h_s}{6}}{h_s \pi^2} \sin\frac{\pi x}{L_x}\left(\dot{u}_f + \frac{1}{2}\dot{w}_f^2\right) \end{bmatrix} dx = 0, \tag{15}$$

$$\frac{\partial \Pi}{\partial \Delta} = FL_x - 2(D + Q_{11}^s h_s - Q_{12}^s h_s \nu_x)\Delta + \int_0^{L_x} \begin{bmatrix} 2D\left(\dot{u}_f + \frac{1}{2}\dot{w}_f^2\right) + (Q_{11}^s h_s \\ -Q_{12}^s h_s \nu_x)\left(\dot{u}_f + \frac{1}{3}\dot{w}_f^2\right) \end{bmatrix} dx = 0. \tag{16}$$

Coefficients (q_s, q_t and Δ) in Eqs. (12) and (13) do not remain constant, which is controlled by integral constraints (Eqs. (14)–(16)). Therefore, Eqs. (12) and (13) belongs to a variable-coefficient differential equations and the wrinkling evolution can be described without any phenomenological or number assumptions.

With the assumption of simple supports at both ends, the boundary conditions can be expressed as:

$$w_f(0) = \ddot{w}_f(0) = 0, \tag{17}$$

$$w_f(L) = \ddot{w}_f(L) = 0. \tag{18}$$

In addition, more complicated boundary conditions arise for matching the applied stress at the ends:

$$\left(4D + \frac{4Q_{11}^s h_s}{3}\right)\dot{u}_f(0) + (4D + Q_{11}^s h_s)\frac{1}{2}\dot{w}_f^2(0) + F - (4D + 2Q_{11}^s h_s - 2Q_{12}^s h_s \nu_x)\Delta = 0. \tag{19}$$

Here we try to solve the buckling governing equations based on half of the length due to deformation symmetry along the length direction. The boundary conditions at $z = L/2$ are:

$$\dot{w}_f(L/2) = \dddot{w}_f(L/2) = u_f(L/2) = 0. \tag{20}$$

3. Numerical solution method

The numerical continuation algorithm is used to solve the resulting non-linear Eqs. (12)–(16). This approach, known as path-following technique, starts from an initial solution. A free parameter is introduced to observe how solutions evolve. It mainly allows for a systematic exploration of the equilibria, giving a detailed description of the different types of behaviors (bifurcation, fold, etc.) that the system may exhibit in dependence of the key parameters. Further details can be found in the reference Doedel et al. (1991).

In this paper, the main advantage of the numerical continuation method is its ability to detect bifurcation points and switch branch. Here, the governing equations belong to the family of non-autonomous fourth-order ordinary differential boundary value problems with integral constraints. Although the numerical continuation method is usually employed to compute solutions of autonomous systems, non-autonomous equations (Eqs. (12)–(16)) can be solved by introducing another variable x, which transforms a sixth-order non-autonomous system into a seventh-order autonomous system.

Note that compared to other methods, this method does not need the introduction of any phenomenological assumptions or imperfections. Key features, such as the wavelength of buckling on the compressed side, develop gradually during evolution of the system from the undeformed state rather than in a more abrupt way.

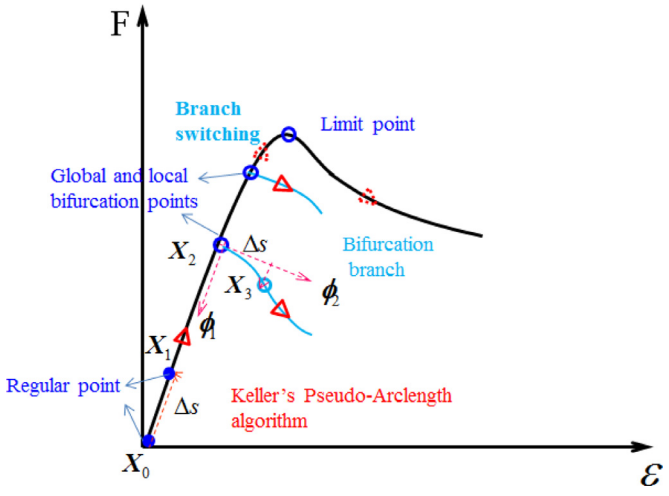

Fig. 2. Path-following strategy of the continue algorithm in the case where bifurcation branches lie before the limit point.

3.1. Path-following technique

Let us rewrite Eqs. (12) and (13) as a generalized non-linear problem as:

$$\nabla \Pi(\boldsymbol{c}, \boldsymbol{p}) = \boldsymbol{f}(\boldsymbol{c}, \boldsymbol{p}) = \boldsymbol{0}. \tag{21}$$

where $\boldsymbol{c} = \{w_f, u_f\}$ represents a vector of unknown variables, and $\boldsymbol{p} = \{F, q_s, q_t, \Delta\}$ represents a vector of control parameters.

As mentioned above, an equilibrium path can be traced starting from the initial non-deformed state $\boldsymbol{X}_0$ ($(\boldsymbol{c}_0, p_0)$) through the continuous change of a leading parameter ($p = F$ is chosen in the current case). Keller's Pseudo-Arclength algorithm is used here, such that computations can be performed past where a fold is encountered. This method computes the new continuation step$\boldsymbol{X}_1$ ($(\boldsymbol{c}_1, p_1)$), as a solution to the following equations (Fig. 2):

$$\begin{aligned} &\boldsymbol{f}(\boldsymbol{c}_1, p_1) = 0 \\ &(\boldsymbol{c}_1 - \boldsymbol{c}_0)^* \boldsymbol{c}_0' + (p_1 - p_0)p_0' - \Delta s = 0 \end{aligned} \tag{22}$$

where * denotes vector's transpose, $(\boldsymbol{c}_0', p_0')$is the tangent vector at $(\boldsymbol{c}_0, p_0)$ and Δs is the size of the continuation step. Note that, the stepsize Δs should be sufficiently small (e.g. 10^{-2} or 10^{-3}) to insure that the Jacobian matrix is full rank and the bifurcation points in the equilibrium path cannot be left out.

3.2. Detection of bifurcation points and branch switching

Keller's Pseudo-Arclength algorithm works well for tracing the path where only one isolated curve passing through every regular point (solid points in Fig. 2). But it fails at a bifurcation point, at which two distinct branches intersect. The bifurcation point belongs to a simple singular point, which results in the reduction of rank of the Jacobian matrix $\boldsymbol{J}$ by at least one.

$\boldsymbol{X}_2$ is a simple singular point of $\boldsymbol{f}(\boldsymbol{c}, p) = 0$ (hollow points in Fig. 2) and $X(\boldsymbol{s})$ is a solution branch of $\boldsymbol{f}(\boldsymbol{X}) = 0$, where $\boldsymbol{s}$ is some parametrization. Then the following equations can be obtained:

$$\boldsymbol{N}(\boldsymbol{f}_{\boldsymbol{X}}^2) = Span\{\boldsymbol{\phi}_1, \boldsymbol{\phi}_2\}, \quad \boldsymbol{N}(\boldsymbol{f}_{\boldsymbol{X}}^{2*}) = Span\{\boldsymbol{\varphi}\}, \tag{23}$$

where $\boldsymbol{N}$ denotes the nullspace and $\boldsymbol{f}_{\boldsymbol{X}}^2$ represents a short hand for the derivatives of $\boldsymbol{f}$ with respect to $\boldsymbol{c}$ evaluated at $(\boldsymbol{c}_2, p_2)$. Meanwhile, two other equations can be obtained by differentiating$\boldsymbol{f}(\boldsymbol{X}(\boldsymbol{s})) = 0$:

$$\boldsymbol{f}_{\boldsymbol{X}}^0 \boldsymbol{X}_0' = 0, \text{ and } \boldsymbol{f}_{\boldsymbol{X}\boldsymbol{X}}^0 \boldsymbol{X}_0' \boldsymbol{X}_0' + \boldsymbol{f}_{\boldsymbol{X}}^0 \boldsymbol{X}_0'' = 0. \tag{24}$$

Thus $\boldsymbol{X}_0' = \alpha\boldsymbol{\phi}_1 + \beta\boldsymbol{\phi}_2$ can be obtained for $\alpha, \beta \in \mathbf{R}^1$, and following equation can be generated:

$$\boldsymbol{\varphi}^* \boldsymbol{f}_{\boldsymbol{X}\boldsymbol{X}}^2 (\alpha\boldsymbol{\phi}_1 + \beta\boldsymbol{\phi}_2)^2 + \boldsymbol{\varphi}^* \boldsymbol{f}_{\boldsymbol{X}}^2 \boldsymbol{X}_0'' = 0. \tag{25}$$

Since the second term in Eq. (25) is zero, the equation can be rewritten as:

$$k_{11}\alpha^2 + 2k_{12}\alpha\beta + k_{22}\beta^2 = 0, \tag{26}$$

where the value of k are given as $k_{11} = \boldsymbol{\varphi}^* \boldsymbol{f}^2_{\boldsymbol{XX}} \boldsymbol{\phi}_1 \boldsymbol{\phi}_1$, $k_{12} = \boldsymbol{\varphi}^* \boldsymbol{f}^2_{\boldsymbol{XX}} \boldsymbol{\phi}_1 \boldsymbol{\phi}_2$ and $k_{22} = \boldsymbol{\varphi}^* \boldsymbol{f}^2_{\boldsymbol{XX}} \boldsymbol{\phi}_2 \boldsymbol{\phi}_2$. The above equation is the algebraic branching equation (ABE), further details can be found in the reference Keller (1977). If the discriminant is positive, ($k_{12}^2 - k_{11}k_{22} > 0$), then the ABE has two distinct real nontrivial solution pairs (α_1, β_1) and (α_2, β_2), which are unique up to scaling. In such case, $\boldsymbol{X}_2$ is detected as a bifurcation point, which gives rise to path bifurcation. When the trajectories of the branching paths from a bifurcation point are well defined, switching between these separated branches is possible, such that parameter continuation can be performed along the alternative paths.

Then the first solution, $\boldsymbol{X}_3$, on the bifurcating branch can be computed from:

$$\boldsymbol{f}(\boldsymbol{X}_3) = 0, \tag{27}$$

$$(\boldsymbol{X}_3 - \boldsymbol{X}_2)^* \boldsymbol{\phi}_2 - \Delta s = 0, \tag{28}$$

where $\boldsymbol{\varphi}_2 \perp \boldsymbol{\varphi}_1$, and $\boldsymbol{\varphi}_1$ is taken as the direction of the "given " branch at the branch point, i.e., $\boldsymbol{\phi}_1 = \boldsymbol{X}_2'$ and graphical interpretation is shown in Fig. 2.

As aforementioned, the bifurcation point leads to singularity and results in the rank of the Jacobian matrix $\boldsymbol{J}$ reduction by at least one. Therefore, the critical global buckling load, F_g, at which $q_s = q_t = w_f = u_f = 0$, occurs when the following matrix is singular:

$$\begin{vmatrix} \dfrac{\partial^2 \Pi}{\partial q_s \partial q_s} & \dfrac{\partial^2 \Pi}{\partial q_s \partial q_t} \\ \dfrac{\partial^2 \Pi}{\partial q_t \partial q_s} & \dfrac{\partial^2 \Pi}{\partial q_t \partial q_t} \end{vmatrix} = 0. \tag{29}$$

Hence the critical load for global buckling, F_g, is obtained as:

$$F_g = \frac{EI\pi^2}{L_x^2} + \frac{2Q^s_{33} h_s^3 \pi^2}{L_x^2} \left(\frac{\frac{D}{2} + \frac{Q^s_{11} h_s}{6}}{2Q^s_{33} h_s + \frac{h_s^2 \pi^2}{L_x^2} \left(\frac{D}{2} + \frac{Q^s_{11} h_s}{6} \right)} \right). \tag{30}$$

4. Results and discussions

Numerical solutions for a typical film/substrate system comprising a Si film ($E_f = 1.3 \times 10^5$MPa, $\nu_f = 0.3$) and a PDMS substrate ($E_x = E_y = 1.8$MPa, $\nu_f = 0.48$) with a length and width of 1.5 mm are acquired by solving the nonlinear equations (Eqs. (12)–(16)). The shear modulus, G_i, is 0.61 MPa for an isotropic substrate. The numerical investigation of buckling mode is conducted for the cases, where either global or local buckling is critical. The principal parameters used in the continuation process are interchangeable, but generally F is varied for computing the equilibrium paths for the distinct buckling modes. The continuation process initiated from zero load along the pre-buckling equilibrium path until a bifurcation point is found. Both of the local buckling load, F_l, and global buckling load, F_g, are obtained numerically, while the global critical buckling load can be validated based on Eq. (30).

Local wrinkling occurs when its critical load is smaller than its counterpart for global buckling, i.e., $F_l < F_g$, while global buckling occurs when the opposite holds. Fig. 3 shows the ratio of local to global critical buckling load, F_l/F_g, versus the ratio of substrate to film thickness, h_s/h_f.

Two different instability modes and corresponding morphologies may occur with different thickness ratios. The global buckling load increases more significantly with the substrate thickness increment compared to the local buckling load. For a small substrate thickness ($h_s/h_f < 250$) such that $F_l/F_g > 1$, global buckling occurs,

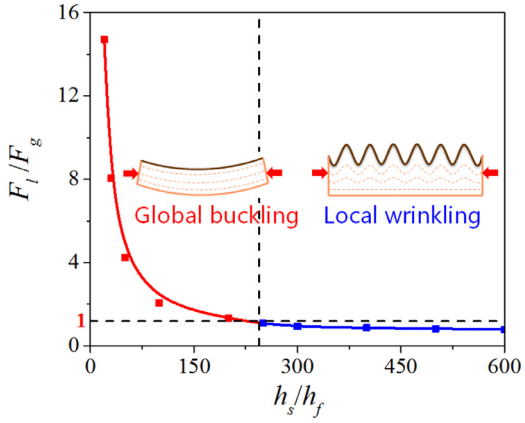

Fig. 3. Relationship between the ratio of local to global critical buckling load and the thickness ratio of substrate to film.

while local wrinkling occurs for a thick substrate ($h_s/h_f > 250$). The critical thickness ratio is very close to the result in Wang et al. (2008). In order to investigate the different post-buckling evolution behaviors of the two different modes, which often leads to complicated responses with surface morphology transitions, two different ratios of thickness, h_s/h_f=100, 300, are adopted, respectively. In addition, the principle parameter is normalized with respect to the global buckling load ($\eta = F/F_g$) in the following calculations. In this case, when global buckling is critical, the first bifurcation occurs around the dimensionless load parameter η=1, while the first bifurcation occurs around $\eta < 1$, when local buckling is critical.

4.1. Critical global buckling

As aforementioned, the global buckling is critical, when the thickness ratio reaches h_s/h_f=100. The relationship between the dimensionless load parameter and total end-shortening ($\eta - \varepsilon$) is shown in Fig. 4(a).

As seen from Fig. 4(a), point B (ε=0.001) is the first bifurcation point, where post-buckling path bifurcates from the primary equilibrium path. The critical absolute value is 0.053 N/mm, which agrees well with the result in Xu et al., (2014) (about 0.052 N/mm) considering the same geometric and material properties. When ε is smaller than 0.001 (section AB), both global and local deformations are negligible ($q_s = q_t = w_f = u_f \approx 0$), which can be seen from Fig. 4(b) (grey line). The post-buckling path is then computed from the first bifurcation (point B) by aforementioned branch switching, and small step size Δs is chosen (e.g. 10^{-3}) to insure that the second bifurcation point not to be ignored. Many subsequent bifurcation points are detected on the weakly stable post-buckling path and the focus is on the one with the lowest value of F. The distinct post-buckling equilibrium path is traced until the second bifurcation point is founded (point C). The load parameter, η, remains almost unchanged with $0.001 < \varepsilon < 0.0036$ (section BC), and the low-strain phase characterized by smooth global buckling mode acts as a dominant role without any local wrinkling, namely $w_f = u_f = 0$. Since the global mode is only weakly stable, no significant post-buckling stiffness is exhibited initially. Therefore, Eqs. (15) and (16) can be simplified as the following equations, which describe the relationship of free parameters (q_s, q_t and Δ):

$$q_s = \left(\frac{h_s^2 \pi^2 (D/2 + Q^s_{11} h_s/6)}{2Q^s_{33} L_x^2} + 1 \right) q_t, \tag{31}$$

$$\Delta = \frac{F_g L_x}{2(D + Q^s_{11} h_s - Q^s_{12} h_s \nu_x)}. \tag{32}$$

When ε is in the range of (0.0036, 0.007) (section CD), the high-strain phase characterized by local wrinkling ripple deforma-

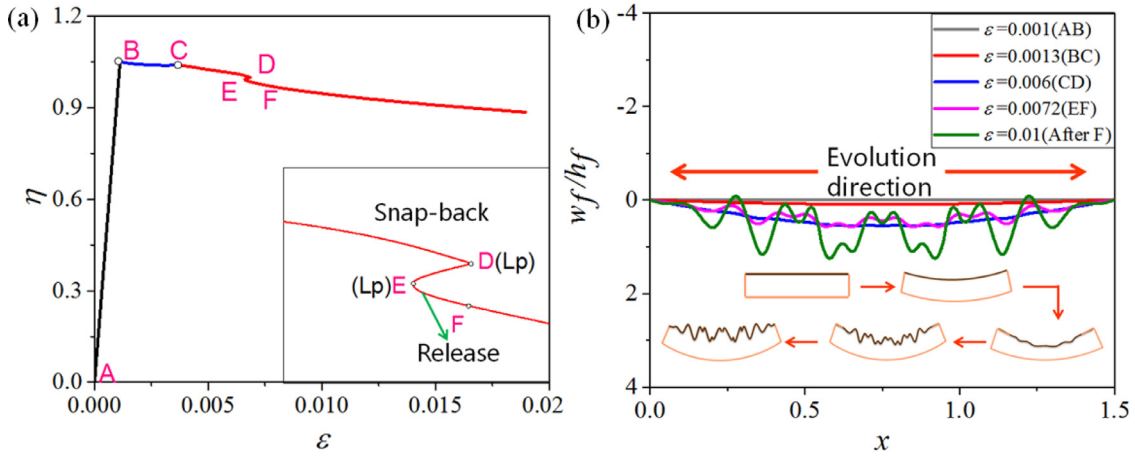

Fig. 4. Equilibrium path and instability mode transition for global critical case (h_s/h_f=100): (a) Relationship between the dimensionless load parameter and total end-shortening; (b) Instability modes in different stages.

tion occurs in the middle of system, although the low-strain phase still exists. Therefore, the morphology at this stage exhibits a so-called mixed-curvature stage with a combination of smooth global buckling and local wrinkling deformation (Wang et al., 2016).

With the compressive strain increasing, two limit points (D, E) are encountered and a snap-back characters the interactive post-buckling path, even only for a relative narrow range ($\Delta\varepsilon=2\times10^4$). The snap-back indicates a process from destabilization to restabilization, where the morphology of film jumps from a sinusoidal wrinkling mode (the blue line in Fig. 4(b)) into a doubling-period wrinkling mode (the purple line in Fig. 4(b)) in the middle of the film. Here, the destabilization is derived from the interaction of global and local buckling modes and the restabilization arises from the inherent stretching that occurs during film buckling owing to large deflections, which accounts for its significant post-buckling stiffness (Koiter and Pignataro, 1976; Wadee and Gardner, 2012). Brau et al. (2011) also have shown that the sinusoidal wrinkling mode can evolve into the doubling-period wrinkling morphology under a large compressive strain.

In section DF, the system needs an effective configurational transition to release the high in-plane strain energy. Since the in-plane stiffness in the bilayer system is much higher than the out-of-plane stiffness, the doubling-period wrinkling deformation represents an effective configurational transition to release the in-plane strain energy, which leads to an energetically favorable state at sufficiently global sway. As such, the in-plane strain energy release is the driving force for doubling-period wrinkles.

When ε is larger than 0.007 (after point F), the morphology of system is a combination of global buckling, sinusoidal local wrinkling and doubling-period wrinkling. With the increase of compressive strain, the sinusoidal local wrinkling mode spreads towards the ends of the film and evolves along the depth direction, resulting in a constant wrinkling wavelength and increasing wrinkling amplitude. Besides, further loading increment would lead to global restabilization of the system, which may occur as a result of the boundaries confining the spread of the buckling morphology any further.

Fig. 5(a) depicts the bifurcation paths of different characteristic positions in the film. The change in sign of the out-of-plane displacement from the primary path clearly demonstrates the evolution of instability again. Note that all the bifurcation paths distribute on the positive of x-axis without intersecting with the primary path due to the effect of global buckling deformation. Wrinkles first generate in the middle of the film with a sudden jump of the bifurcation path (red and blue line in Fig. 5(a)) after passing through the second bifurcation point (point C). It can also be demonstrated form Fig. 5(b), which depicts the distribution of axial strain ε_x of the film along the longitudinal direction. Here, the critical strain of sinusoidal wrinkles (dashed line in Fig. 5(b)) based on classical linearized stability analysis was presented in Chen and Hutchinson (2004), with Föppl-von Kármán nonlinear elastic plate assumption for the film. Subject to uniaxial in-plane compression, the critical strain for the onset of local wrinkling instability is expressed as:

$$\varepsilon_c = \frac{1}{4}\left(\frac{3E_s(1-\nu_f)}{E_f(1-\nu_s)}\right)^{2/3}. \tag{33}$$

As seen from Fig. 5(b), only the membrane strains in the middle region ($0.2 < x < 1.3$) exceed the critical strain (dashed line) in section CD, which indicates that local wrinkles form from the middle of the film rather than from the edges. Besides, there is a slight fluctuation and snap-back in the bifurcation paths, on which the characteristic points are all located in the middle wrinkling region in section DE. After point E, a sudden jump (0.35 displacement) is observed from the bifurcation path of point ($x=0.2$), and the membrane strains on the edges are beyond the critical value, which is demonstrated as the occurrence of new wrinkles. Meanwhile, the distribution of membrane strain is similar to the local wrinkling morphology due to a higher wrinkling degree and the last term $\frac{1}{2}\dot{w}^2$ gradually acts a dominant role in Eq. (5). All these results also reveal that the fluctuated wrinkles in the stressed regions promote the wrinkling spread from the middle to edges.

4.2. Critical local wrinkling

In this section, the film/substrate system with a thickness ratio, h_s/h_f=300, is analyzed following the aforementioned strategy. As seen from Fig. 6(a), the dimensionless load parameter, η=0.93 < 1, corresponding to the first bifurcation point (point b), which indicates that the local wrinkling is critical. Compared to the global critical case, the local critical case has snap-back occurring immediately after the first bifurcation point in the post-buckling path. The emergence of this snap-back corresponds to the formation of a new wrinkling, which is similar to the global buckling case. Thus, it is not presented here in detail for brevity.

Meanwhile, the evolution of wrinkling patterns is illustrated in Fig. 6(a), (b). Different from the global case, first instability mode is localized near the boundary with an unobvious global deformation.

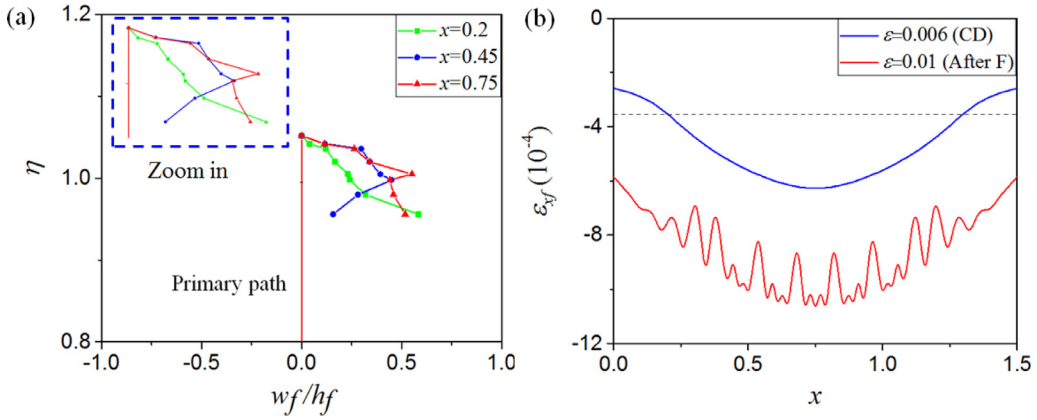

Fig. 5. Bifurcation paths and axial strain distribution for global critical case (h_s/h_f=100): (a) Bifurcation paths of different characteristic positions in the film; (b) Distribution of axial strain of the film along the longitudinal direction.

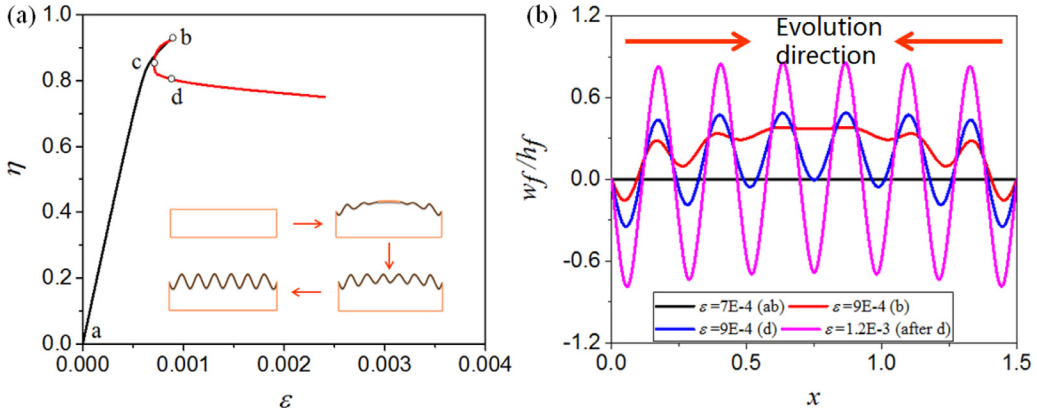

Fig. 6. Equilibrium path and instability mode transition for local critical case (h_s/h_f= 300): (a) Relationship between the dimensionless load parameter and total end-shortening; (b) Instability modes in different stage.

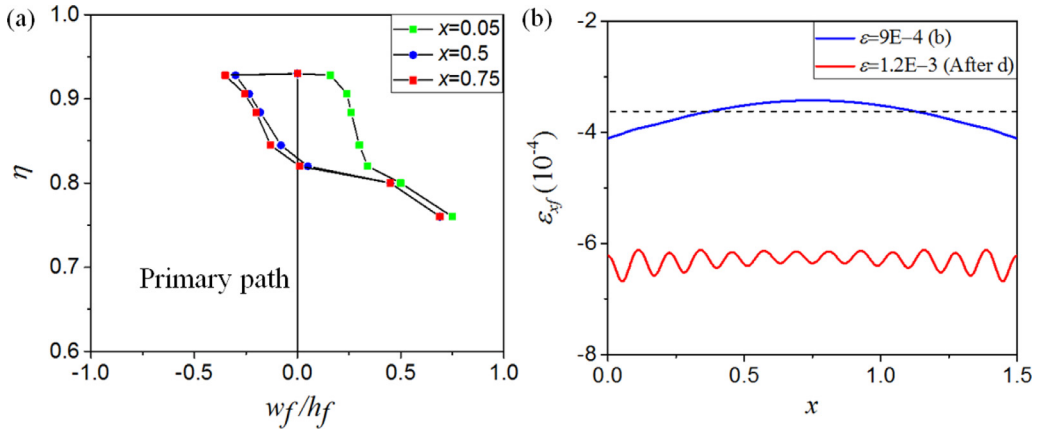

Fig. 7. Bifurcation paths and axial strain distribution for global critical case (h_s/h_f=100): (a) Bifurcation paths of different characteristic positions in the film; (b) Distribution of axial strain of the film along the longitudinal direction.

Boundary effects are important at the first appearance of wrinkles, and then local wrinkles spread from boundary edges to the middle. The sinusoidal pattern gradually tends to be uniform with $\varepsilon >$ 9E − 4.

Figs. 7(a), (b) depicts the bifurcation paths of different characteristic positions and membrane strain of the film. As seen from Fig. 7(b), only the membrane strains near the boundary ($x > 0.36$,$x < 1.14$) exceed the critical strain (dashed line) at the first bifurcation point, which demonstrates that local wrinkles form from the edges of the film rather than from the middle. Boundary effects appear due to stress concentration in these areas. Then the local wrinkling mode grows, spreads towards the middle and tends to be more apparent with respect to the increasing strain. Both the bifurcation paths of points in the middle region (at x=0.5 and x=0.75) show a snap-back and interaction with the primary path, which indicates the occurrence of a new wrinkle (Fig. 7(a)). After point d, the wrinkles reenter a relatively stable growing state, which is stopped by the limitations of system geometry and its elastic loading. Note that some of the responses, i.e. doubling-period wrinkling, cannot be obtained here since this study is

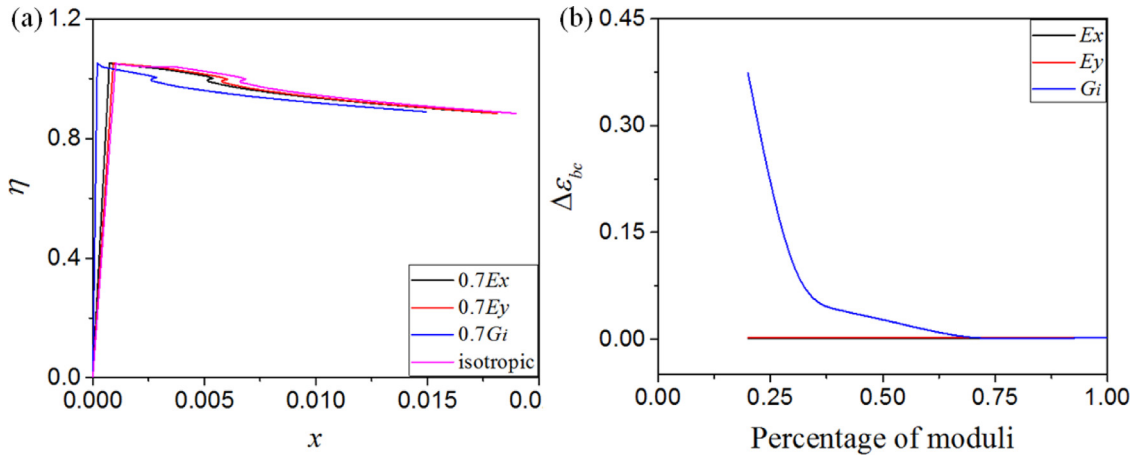

Fig. 8. (a) Equilibrium paths for different moduli in the case of h_s/h_f=100; (b) Relationship between $\Delta\varepsilon_{bc}$ and variation of elastic and shear moduli.

limited to a 2D system with relatively small compression strains in the substrate.

4.3. Orthotropic substrate

In this section, we focus on discussing the effects of orthotropic substrate on the global and local buckling behaviors of the system. Fig. 8(a) shows the equilibrium paths for different moduli in the case of h_s/h_f=100, while Poisson ratio is kept as a constant.

The post-buckling path of orthotropic substrate follows almost similar trend of the isotropic one. Compared to the isotropic substrate, the main difference, affected by anisotropy, lies in the locations of the first and second bifurcation. Here, we define the total end-shortening corresponding to the first bifurcation as ε_b, and the distance between the first and second bifurcation as $\Delta\varepsilon_{bc}$. Fig. 8(b) depicts the relationship between $\Delta\varepsilon_{bc}$ and variation of elastic and shear moduli.

It can be seen from the figures that elastic moduli (E_x,E_y) only slightly affects the end-shortening corresponding to the first bifurcation, and has little, if any, impact on the distance between the first and second bifurcation$\Delta\varepsilon_{bc}$. However, ε_b and $\Delta\varepsilon_{bc}$, especially the latter one, show a strong dependence on the variation of shear modulus. As seen from Fig. 8(b), the distance between the first and second bifurcation increases from 2.6E-3 to 0.37 with the decrease of shear modulus from $1G_i$ to 0.2 G_i and reaches its minimum of ca. 2.5E-4 at 0.7 G_i.

The distance between the first and second bifurcation, $\Delta\varepsilon_{bc}$, can be approximately expressed as follows based on Eq. (31). We can deduce from Eq. (34) that the shear modulus can enhance the shearing stiffness ($Q^s_{33}h_s$) and the tilt q_t, resulting in a nonlinear effect on the global buckling critical load. Nevertheless, the effect of elastic moduli (E_x,E_y) on $\Delta\varepsilon_{bc}$ is negligible due to an extremely large ratio of stiffness ($D/Q^s_{11}h_s \approx 10^5$),

$$\Delta\varepsilon_{bc} \propto \frac{\pi^2}{4}\left(\frac{h_s^2\pi^2(D/2+Q^s_{11}h_s/6)}{2Q^s_{33}L_x^2}+1\right)^2 q_t. \tag{34}$$

The above results also indicate that the shear modulus has a great effect on the post-buckling behavior by taking the global buckling and interactive bifurcation loads closer or further and thereby tuning the post-buckling morphology of the film/substrate system.

Fig. 9(a) shows the relationship between the ratio of local to global critical buckling load and variation of shear modulus in the case of h_s/h_f=300. It can be seen that the shear modulus increases from 0.3 G to 1.5 G, when the dimensionless load parameter, η, decreases from 1.52 to 0.84. Meanwhile, when G is larger than 0.88, the local wrinkling is critical and local wrinkling dominates the post-buckling characteristics; while the global buckling is critical and global and local interactive mode is dominant when G is smaller than 0.88. This is because the system loses shear resistance with the decrease of shear modulus and the global mode tends to pure sway with no tilt, which implies that there are little or no differential compression in the film and hence little or no tendency for the response to localize on one face.

In addition, a cross-correlation coefficient, δ, is defined as the ratio of shear strain to compress strain ($\delta=\gamma_3/\varepsilon_f$) to reflect the coupling degree. Fig. 10(a), (b) describe the distributions of shear strain and cross-correlation coefficient for global and local cases.

As seen from the figures, shear strain acts a dominant role, and a strong coupling behavior of compression and shearing occurs near the boundary edges in both cases. Compared to the global critical case, the cross-correlation coefficient of the local critical case near the boundary almost remains constant due to the negligible global effects.

All these results confirm the fact that shears modulus has a decisive effect on the post-buckling behavior especially on the system with a large modulus ratio. Therefore, from the design point of view, it provides another effective method to tune the different micro morphologies of the film/substrate system by changing shear modulus of substrate.

5. Conclusion

In this paper, we ascribe the global and local buckling behaviors of film/substrate systems under compression to the fourth-order nonlinear ordinary differential equations with integral conditions. The equations are solved them by using a continuation algorithm. The presented results heavily rely on this robust path-following technique that is able to detect secondary bifurcations and to trace a non-linear post-buckling path. The critical condition for local and global buckling with respect to different thickness ratios is investigated. Meanwhile, the occurrence and evolution of global and local buckling modes have been observed. Second bifurcation and snap-back phenomenon character both the equilibrium paths in the post-buckling range, which can be seen as markers of the evolution of instability modes. As for a global critical case, the buckling mode is a result of global and local instability interaction, and local wrinkling first forms in the middle of systems and spreads to the boundary edges. Different from the global critical case, wrinkling first occurs near the boundary edges and spread to the middle for a local critical case. In addition, shear modulus of an orthotropic substrate acts as a dominant role in the bifurcation

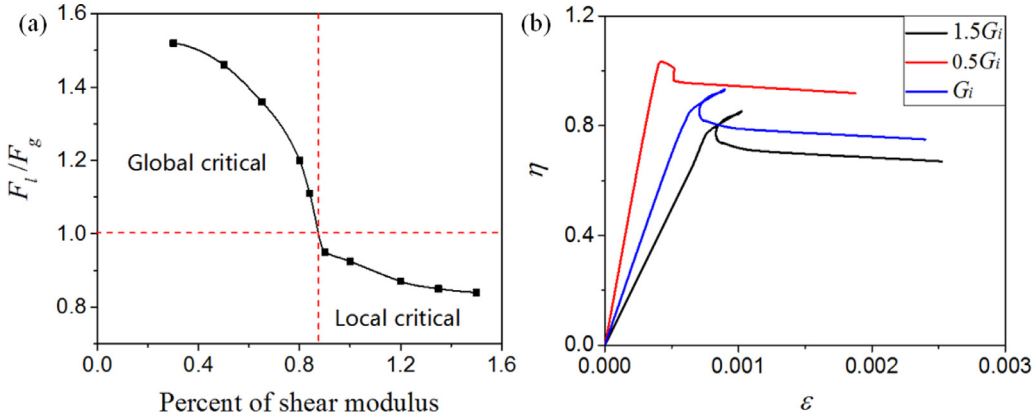

Fig. 9. (a) Relationship between the ratio of local to global critical buckling load and the variation of shear modulus; (b) Equilibrium paths for different shear modulus in the case of h_s/h_f= 300.

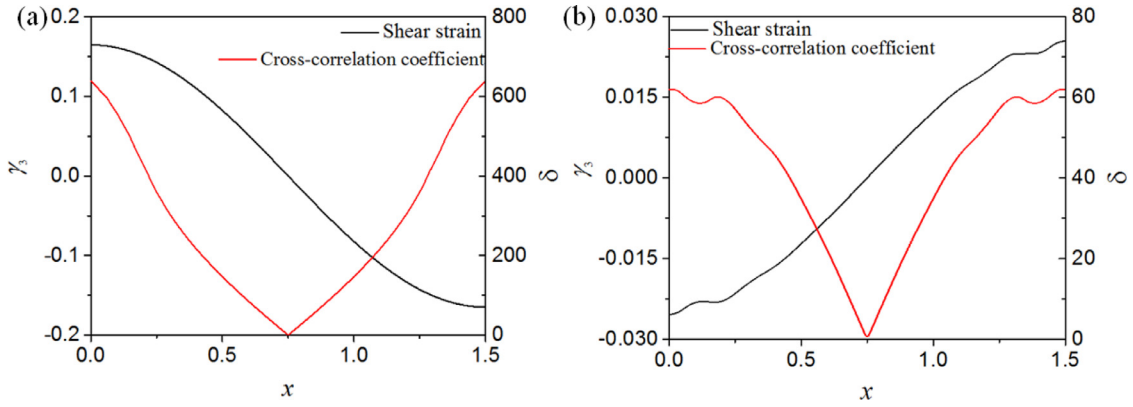

Fig. 10. Distributions of shear strain and cross-correlation coefficient for global and local critical cases: (a) Global critical case (ε=0.006); (b) Local critical case (ε=9E−4).

portrait, which can maximize the interaction between local and global buckling and decide the instability modes. Therefore, from the design point of view, it provides another effective method to tune the different micro morphologies of the film/substrate system by changing shear modulus of substrate.

Acknowledgments

The authors gratefully acknowledge financial supports from National Natural Science Foundation of China, 11172079 and 11572099; Program for New Century Excellent Talents in University, NCET-11-0807; Natural Science Foundation of Heilongjiang Province of China, 40000045-6-15441; the Fundamental Research Funds for the Central Universities, HIT.BRETIII.201209, HITMK-STISP.201629. Meanwhile, we thank Prof. Nan Wu from University of Manitoba, Dr. J. Al-Ghalith from University of Minnesota, Dr. L. Bai in Shanghai Jiao Tong University for their great help.

References

Abichou, H., Zahrouni, H., Potier-Ferry, M., 2002. Asymptotic numerical method for problems coupling several nonlinearities. Comput. Methods Appl. Mech. Eng. 191, 5795–5810.
Audoly, B, Boudaoud, A, 2008. Buckling of a stiff film bound to a compliant substrate—Part I: formulation, linear stability of cylindrical patterns, secondary bifurcations. J. Mech. Phys. Solids 56 (7), 2401–2421.
Bai, L., Wadee, M.A., 2015. Mode interaction in thin-walled I-section struts with semi-rigid flange–web joints. Int. J. Nonlin. Mech. 69, 71–83.
Bowden, N., Brittain, S., Evans, A.G., Hutchinson, J.W., Whitesides, G.M., 1998. Spontaneous formation of ordered structures in thin films of metals supported on an elastomeric polymer. Nature 393, 146–149.
Brau, F., Vandeparre, H., Sabbah, A., Poulard, C., Boudaoud, A., Damman, P., 2011. Multiple-length-scale elastic instability mimics parametric resonance of nonlinear oscillators. Nat. Phys. 7, 56–60.
Cai, S., Breid, D., Crosby, A.J., Suo, Z., Hutchinson, J.W., 2011. Periodic patterns and energy states of buckled films on compliant substrates. J. Mech. Phys. Solids 59, 1094–1114.
Cao, Y., Jia, F., Zhao, Y., Feng, X., Yu, S., 2012. Buckling and post-buckling of a stiff film resting on an elastic graded substrate. Int. J. Solids Struct. 49, 1656–1664.
Chen, X., Hutchinson, J.W., 2004. Herringbone buckling patterns of compressed thin films on compliant substrates. J. Appl. Mech. 71, 597–603.
Damil, N., Potier-Ferry, M., 1990. A new method to compute perturbed bifurcation: application to the buckling of imperfect elastic structures. Int. J. Eng. Sci. 26, 943–957.
Doedel, E.J., Keller, H.B., Kernévez, J.P., 1991. Numerical analysis and control of bifurcation problems (I): bifurcation in finite dimensions. Int. J. Bifurcat. Chaos 1 (3), 493–520.
Efimenko, K., Rackaitis, M., Manias, E., Vaziri, A., Mahadevan, L., Genzer, J., 2005. Nested self-similar wrinkling patterns in skins. Nat. Mater. 4, 293–297.
Harrison, C., Stafford, C.M., Zhang, W.H., Karim, A., 2004. Sinusoidal phase grating created by a tunably buckled surface. Appl. Phys. Lett. 85 (18), 4016–4018.
Huang, R., Suo, Z., 2002. Instability of a compressed elastic film on a viscous layer. Int. J. Solids Struct. 39 (7), 1791–1802.
Im, S.H., Huang, R., 2008. Wrinkle patterns of anisotropic crystal films on viscoelastic substrates. J. Mech. Phys. Solids 56, 3315–3330.
Ke, L., Ruess, M., Abdalla, M., 2016. An eigenanalysis-based bifurcation indicator proposed in the framework of a reduced-order modeling technique for nonlinear structural analysis. Int. J. Nonlin. Mech. 81, 129–138.
Keller, H.B., 1977. Numerical solution of bifurcation and nonlinear eigenvalue problems. In: Rabinowitz, P. (Ed.), 'Applications of Bifurcation Theory'. Academic Press, New York, pp. 359–384.
Koch, K., Bhushan, B., Jung, Y.C., Barthlott, W., 2009. Fabrication of artificial Lotus leaves and significance of hierarchical structure for superhydrophobicity and low adhesion. Soft Mat 5, 1386–1393.
Koiter, W.T. & Pignataro, M. 1976. A General Theory for the Interaction Between Local and Overall Buckling of Stiffened Panels. Technical Report. WTHD 83, Delft University of Technology, Delft, The Netherlands.
Li, B., Cao, Y.P., Feng, X.Q., Gao, H., 2012. Mechanics of morphological instabilities and surface wrinkling in soft materials: a review. Soft Mat 8 (21), 5728–5745.
Pirrera, A, Avitabile, D, Weaver, PM, 2010. Bistable plates for morphing structures: a refined analytical approach with high-order polynomials. Int. J. Solids Struct. 47 (25), 3412–3425.

Rogers, J.A., Someya, T., Huang, Y., 2010. Materials and mechanics for stretchable electronics. Science 327, 1603–1607.
Stafford, C.M., Harrison, C., Beers, K.L., Karim, A., Amis, E.J., Vanlandingham, M.R., Kim, H.-C., Volksen, W., Miller, R.D., Simonyi, E.E., 2004. A buckling-based metrology for measuring the elastic moduli of polymeric thin films. Nat. Mater. 3, 545–550.
Schweikart, A., Fery, A., 2009. Controlled wrinkling as a novel method for the fabrication of patterned surfaces. Microchim. Acta 165, 249–263.
Sun, J.Y., Xia, S., Moon, M.W., Oh, K.H., Kim, K.S., 2012. Folding wrinkles of a thin stiff layer on a soft substrate. Proc. R. Soc. A 468, 932–953.
Xu, F., Potier-Ferry, M., Belouettar, S., Cong, Y., 2014. 3D finite element modeling for instabilities in thin films on soft substrates. Int. J. Solids Struct. 51 (21), 3619–3632.
Xu, F., Koutsawa, Y., Potier-Ferry, M., Belouettar, S., 2015. Instabilities in thin films on hyperelastic substrates by 3D finite elements. Int. J. Solids Struct. 69, 71–85.
Wadee, M.A., Gardner, L., 2012. Cellular buckling from mode interaction in I-beams under uniform bending. Proc. R. Soc. A 468, 245–268.
Wadee, M.A., Hunt, G.W., 1998. Interactively induced localized buckling in sandwich structures with core orthotropy. J. Appl. Mech. 65 (2), 523–528.
Wadee, M.K., Lloyd, D.J., Bassom, A.P., 2015. On the interaction of uni-directional and bi-directional buckling of a plate supported by an elastic foundation. Proc. R. Soc. A 472, 20150873.
Wang, C.G, Lan, L., Liu, Y.P., Tan, H.F., He, X.D., 2013a. Vibration characteristics of wrinkled single-layered graphene sheets. Int. J. Solid Struct. 50 (10), 1812–1823.
Wang, C.G, Liu, Y.P., Lan, L., Tan, H.F., 2013b. Graphene wrinkling: formation, evolution and collapse. Nanoscale 2013 5 (10), 4454–4461.
Wang, C.G., Liu, Y.P., Al-Ghalith, J., Dumitrică, T., Wadee, M.K., Tan, H.F., 2016. Buckling behavior of carbon nanotubes under bending: from ripple to kink. Carbon 102, 224–235.
Wang, S., Song, J., Kim, D.H., Huang, Y., Rogers, J.A., 2008. Local versus global buckling of thin films on elastomeric substrates. Appl. Phys. Lett. 93 (2), 023126.
Zhuo, L., Zhang, Y., 2015. The mode-coupling of a stiff film/compliant substrate system in the post-buckling range. Int. J. Solid Struct. 53, 28–37.